

Supporting Information

FeNi₃-FeNi₃N – a High-performance Catalyst for Overall Water Splitting

Shuqin Liang,^{1,2†} Meizan Jing,^{2†} Tiju Thomas,³ Jian Liu,² Haichuan Guo,¹ J. Paul

Attfield,⁴ Ali Saad,¹ Hangjia Shen,^{*1} Minghui Yang^{*1}

1. Solid State functional Materials Research Laboratory, Ningbo Institute of Materials Technology and Engineering, Chinese Academy of Sciences, Ningbo 315201, China.

2. State Key Laboratory of Heavy Oil Processing and Beijing Key Lab of Oil & Gas Pollution Control, China University of Petroleum, Beijing 102249, China.

3. Department of Metallurgical and Materials Engineering, and DST Solar Energy Harnessing Center, Indian Institute of Technology Madras, Adyar, Chennai 600036, Tamil Nadu, India.

4. Centre for Science at Extreme Conditions and School of Chemistry University of Edinburgh, King's Buildings, Mayfield Road, Edinburgh, EH9 3JZ, United Kingdom.

† These authors contributed equally to this work.

Experimental Procedures

Materials and chemicals

Nickelnitrate ($\text{Ni}(\text{NO}_3)_2 \cdot 6\text{H}_2\text{O}$) is purchased from Sinopharm Chemical Reagent Co.,Ltd. Ferric Nitrate ($\text{Fe}(\text{NO}_3)_3 \cdot 9\text{H}_2\text{O}$) is purchased from Sinopharm Chemical Reagent Co., Ltd. Cis-9-Octadecenylamine ($\text{C}_{18}\text{H}_{37}\text{N}$) is purchased from Aldrich Chemistry Co. Anal. Chem. Butyl alcohol ($\text{CH}_3(\text{CH}_2)_3\text{OH}$) is purchased from Tianjin Kermel Chemical Reagent Co., Ltd. All of the chemicals are of analytical grade and used without any further purification.

Synthesis of FeNi_3 - FeNi_3N heterostructure

The synthesis of FeNi_3 - FeNi_3N is performed as follows: 4 mmol of $\text{Ni}(\text{NO}_3)_2 \cdot 6\text{H}_2\text{O}$, 1mmol of $\text{Fe}(\text{NO}_3)_3 \cdot 9\text{H}_2\text{O}$ are dissolved in a mixture of 8ml olamine and 20ml n-butanol. After completely dissolution, the solution is transferred into a 50 mL Teflon-lined stainless-steel autoclave. Then the autoclave is sealed and maintained at 100 °C for 10 h to synthesize Ni-Fe precursor. After the system is cooled down naturally to the room temperature, centrifugation is carried out with ethanol (3-4 times), and then centrifugation is done with distilled water until a colorless solution is obtained. Then the product obtained is dried in a freeze dryer for 48h. Finally, the precursor is first calcinated in a tube furnace to 350 °C for 2h at a rate of 5 °C min^{-1} under flowing NH_3 atmosphere. This is followed by heat treatment at 460 °C, for 2 h with a heating rate of 5 °C min^{-1} under NH_3 atmosphere. In addition, the catalysts with different FeNi_3 ratios are synthesized by controlling the temperature.

The synthesis steps of FeNi_3N nanoparticles are the same as FeNi_3 - FeNi_3N , except that the second ammonolysis temperature is 650 °C. The FeNi_3 nanosheets are prepared in the same process as FeNi_3 - FeNi_3N , but calcined under flowing hydrogen/argon (5% H_2).

Physical characterizations

The XRD patterns of the samples are recorded on a MiniFlex600 X-ray diffractometer with Cu K_α radiation. The morphology of the samples is obtained through scanning electron microscopy (SEM; Hitachi S-4800 electron microscopy). The Transmission electron micrographs (TEM images), high-

resolution TEM (HRTEM) and Energy dispersive X-ray spectroscopy (EDS) spectra are recorded using a FEI-TecnaiF20 TEM microscope.

Electrochemical HER and OER measurements

The electrochemical measurement is performed at room temperature using a three-electrode system controlled on a CH Instruments electrochemical workstation (CHI760E) in N₂-purged 1.0 M KOH. A graphite rod and Ag/AgCl electrode are used as counter and reference electrodes, respectively. The glassy carbon electrode with catalyst-loaded is used as the working electrode. (2.0 mg of the catalyst is dispersed in a 250 μ L mixture of Isopropyl alcohol, water and Nafion. After that, 10 μ L of catalyst ink is drop cast and dried onto the working electrode.

All the potentials are referred to with respect to RHE unless otherwise mentioned. Linear sweep voltammetry (LSV) and cyclic voltammetry (CV) are used to determine the catalytic activity towards HER and OER, respectively. Electrochemical impedance spectra (EIS) are adopted to characterize the electrical conductivity and interfacial charge-transfer kinetics towards HER and OER, respectively. The long-term stability experiment is conducted at a static overpotential of 40000 s, and the changes of voltage over time are recorded.

$ECSA=R_f S/m_{cat}$, in which m_{cat} is the mass of catalysts modified on the electrode; S stands for the real surface area of the smooth metal electrode, which is generally equal to the geometric area of glassy carbon electrode (in this work, $S=0.1963\text{ cm}^2$). The roughness factor R_f is estimated from the ratio of double-layer capacitance C_{dl} for the working electrode and the corresponding smooth metal electrode (assuming that the average double-layer capacitance of a smooth metal surface is $20\text{ }\mu\text{F cm}^{-2}$), that is, $R_f=C_{dl}/20\text{ }\mu\text{F cm}^{-2}$. The C_{dl} is determined by measuring the capacitive current associated with double-layer charging from the scan-rate dependence of cyclic voltammetric stripping. The C_{dl} is estimated by plotting the difference of the cathodic and anodic current densities against the scan rate, in which the slope was twice that of C_{dl} .

RHE calibration in 1.0 M KOH is performed in the high purity hydrogen saturated electrolyte with Pt foil as the working electrode and a Pt wire as the counter electrode. Cyclic voltammograms (CVs) are

run at a scan rate of 1.0 mV s^{-1} , and the average of two potentials at which the current cross zero is taken as the thermodynamic potential for the hydrogen electrode reactions. As shown in **Figure S15**, the potential value relative to Ag/AgCl in the experiment is converted into the potential versus the reversible hydrogen electrode (RHE): $E(\text{RHE}) = E(\text{Ag/AgCl}) + 1.01 \text{ V}$.

Electrochemical overall water splitting measurements

The overall water splitting test is conducted in a two-electrode device using FeNi₃-FeNi₃N catalyst as anode and cathode. For the preparing the working electrode, 5.0 mg of the catalyst is dispersed in a 1000 μL mixture of Isopropyl alcohol, water and Nafion. After that, 500 μL of catalyst ink is drop dried onto $1 \text{ cm} \times 1 \text{ cm}$ Ni foam (mass loading 5.0 mg cm^{-2}). Polarization curves of FeNi₃-FeNi₃N/NF is adopted to test the overall-water-splitting performance using a homemade device to measure hydrogen and oxygen production during overall-water-splitting.

The Faraday efficiency is calculated based on the following equation:

$$FE(\%) = \frac{nFV_{\text{gas}}}{ItV_m} \times 100$$

Here n is the reactive electron number, F was the Faraday constant (96485 C mol^{-1}), V_{gas} is the volume of the produced, V_m is the molar volume of gas, I is the current (A), and t is the time (s).

Theoretical calculations

All DFT calculations are performed by using Vienna *ab initio* simulation package (VASP)¹⁻² with Projector Augmented-wave pseudopotentials³⁻⁴. The generalized gradient approximation with Perdew–Burke–Ernzerh of exchange- correlation functional is employed in the calculations including van der Waals corrections⁵. The valence electrons are solved in the plane-wave basis with a cutoff energy of 500 eV. The convergence criteria for the energy calculation and structure optimization are set to $1.0 \times 10^{-5} \text{ eV}$ and a force tolerance of $0.02 \text{ eV/\AA}^{6-7}$, respectively. $5 \times 5 \times 5$ and $3 \times 3 \times 1$ Monkhorst-Pack grid k-points are taken for geometric optimization of bulk and slab models, respectively. All the surface models contain the 2×2 supercell and the vacuum slab of 15 \AA is used for surface isolation to minimize the interaction between distinct slab surfaces.

According to XRD and HRTEM results, FeNi₃N(111) surface⁸ and FeNi₃(111) surface⁷ are chosen for the DFT calculations, which consist of 8 and 4 atomic layers (shown as Figure S16a and Figure S17a). During geometry optimization, the top four or two atom layers are relaxed, while bottom four or two atom layers are fixed in their bulk positions. Based on DFT analyses, for FeNi₃N-FeNi₃ system, the lattice mismatch degree of FeNi₃N and FeNi₃ is 5.48% < 6.00%. Thus, the FeNi₃N-FeNi₃ heterojunctions can be well established (shown as Figure S18a). The top three atom layers are kept relaxed during the structure optimization.

The adsorption free energy of H* ($\Delta G(H^*)$) is usually considered as an effective descriptor for evaluating hydrogen evolution reaction (HER) activity. A $\Delta G(H^*)$ value of 0 eV suggests an optimal balance between the rate of proton reduction and the ease of removal of adsorbed hydrogen from the surface (the closer to zero the $\Delta G(H^*)$ absolute value ($|\Delta G(H^*)|$), the higher the HER activity⁹). The Gibbs free energy hydrogen adsorption ($\Delta G(H^*)$) is obtained by the following equation:

$$\Delta G(H^*) = \Delta E(H^*) + \Delta ZPE - T\Delta S$$

Where $\Delta E(H^*)$ is hydrogen adsorption energy, which is defined by¹⁰

$$\Delta E(H^*) = \Delta E(H \text{ on slab}) - \Delta E(\text{slab}) - \frac{1}{2}\Delta E(H_2)$$

ΔZPE and ΔS are zero point energy change and entropy change of H* adsorption, respectively. $T\Delta S$ and ΔZPE are obtained by following the scheme proposed by Nørskov *et al.*¹¹ Specifically, on account of the neglectable vibrational entropy of H*, ΔS is calculated using:^{10, 12}

$$\Delta S = S(H^*) - \frac{1}{2}S(H_2) \approx -\frac{1}{2}S(H_2)$$

Additionally, the ΔZPE for H* is estimated by

$$\Delta ZPE = ZPE(H^*) - \frac{1}{2}ZPE(H_2)$$

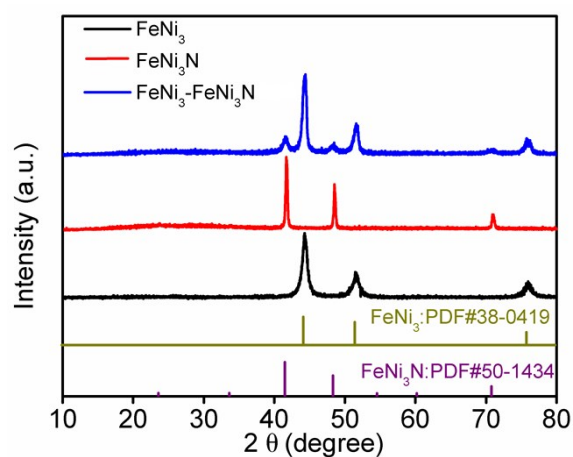


Figure S1. XRD patterns of FeNi_3 , FeNi_3N and $\text{FeNi}_3\text{-FeNi}_3\text{N}$.

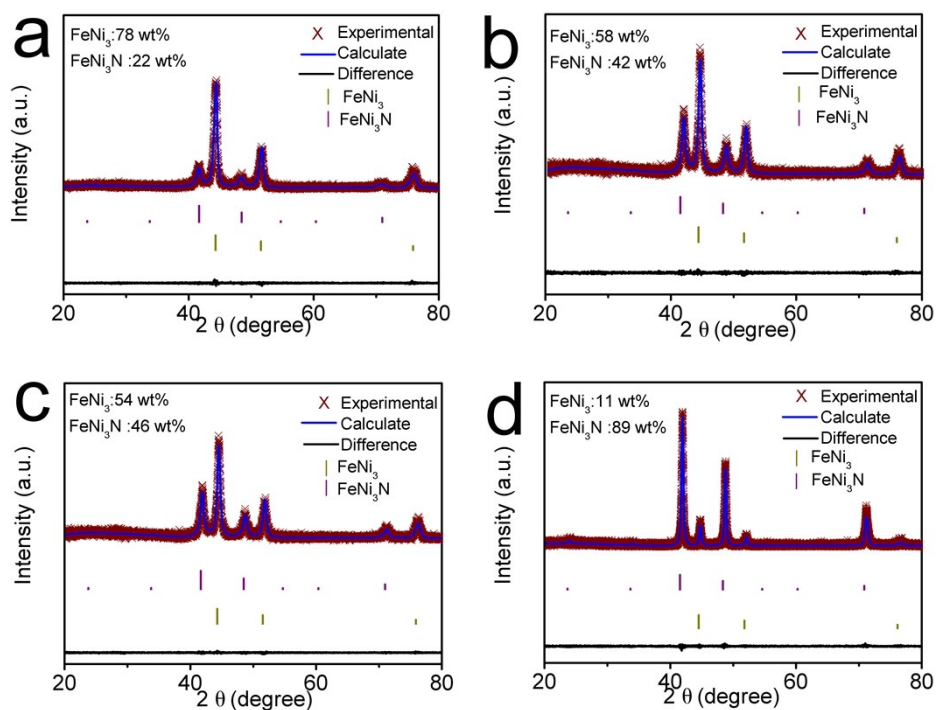


Figure S2. The Rietveld refined XRD pattern of $\text{FeNi}_3\text{-FeNi}_3\text{N}$ at different calcination temperatures. (a) 460 °C, (b) 480 °C, (c) 500 °C (d) 600 °C, respectively.

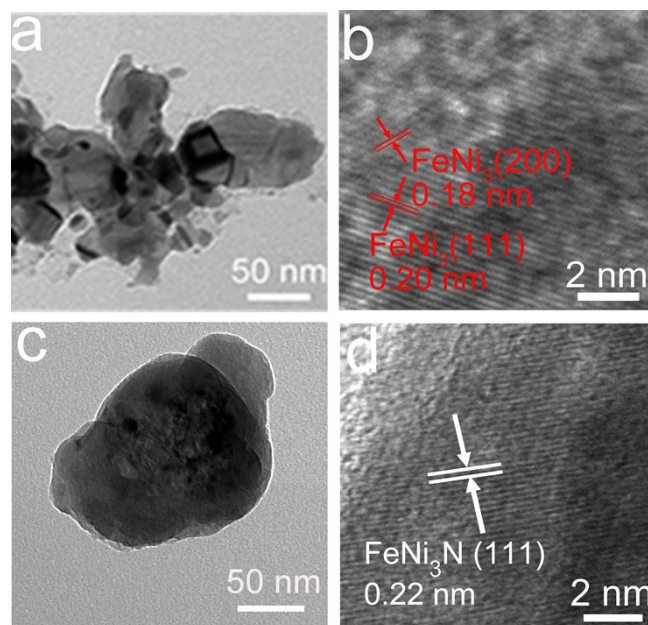


Figure S3. (a-b) TEM and the HRTEM of the FeNi_3 . (c-d) The TEM and HR-TEM of FeNi_3N .

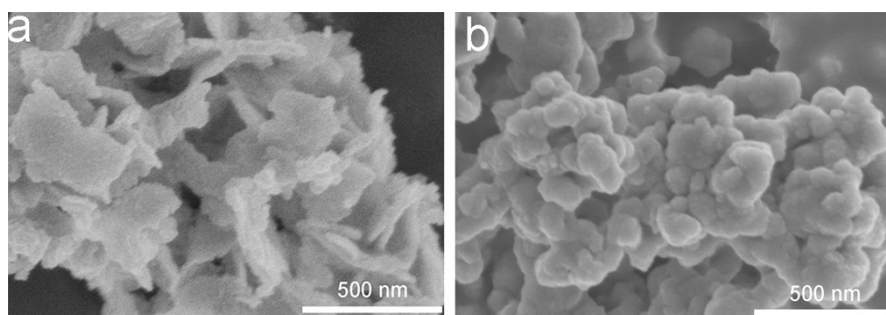


Figure S4. SEM of (a) FeNi_3 , and (b) FeNi_3N .

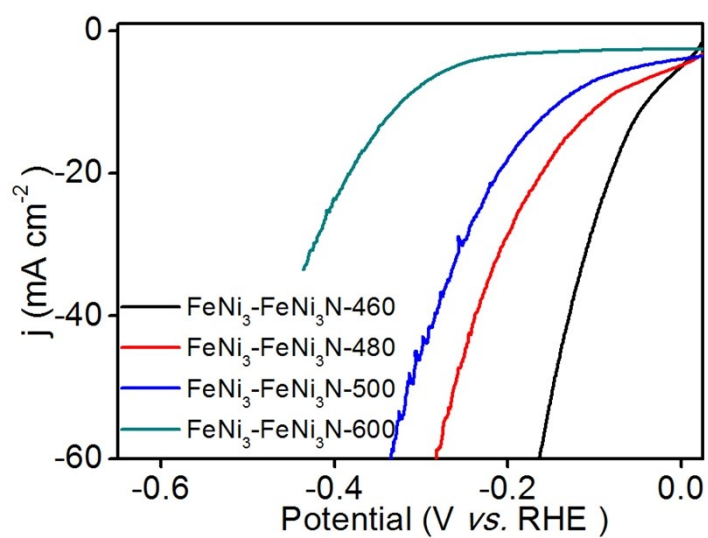


Figure S5. LSV polarization curves of the $\text{FeNi}_3\text{-FeNi}_3\text{N}$ at different calcination temperatures for HER.

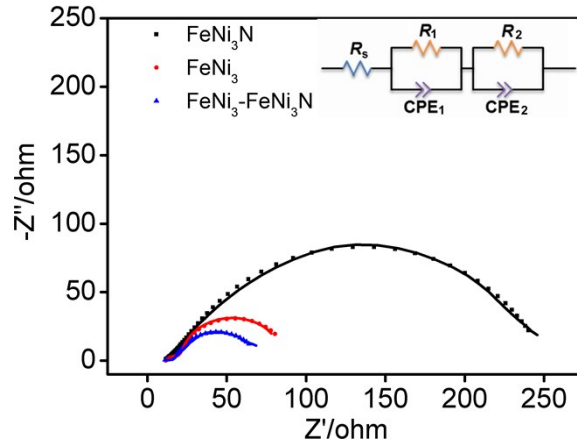


Figure S6. EIS curves of FeNi₃-FeNi₃N, FeNi₃ and FeNi₃N recorded during hydrogen evolution at $\eta = -70\text{mV}$. (R_1 : The material resistance; R_2 : the charge transfer resistance).

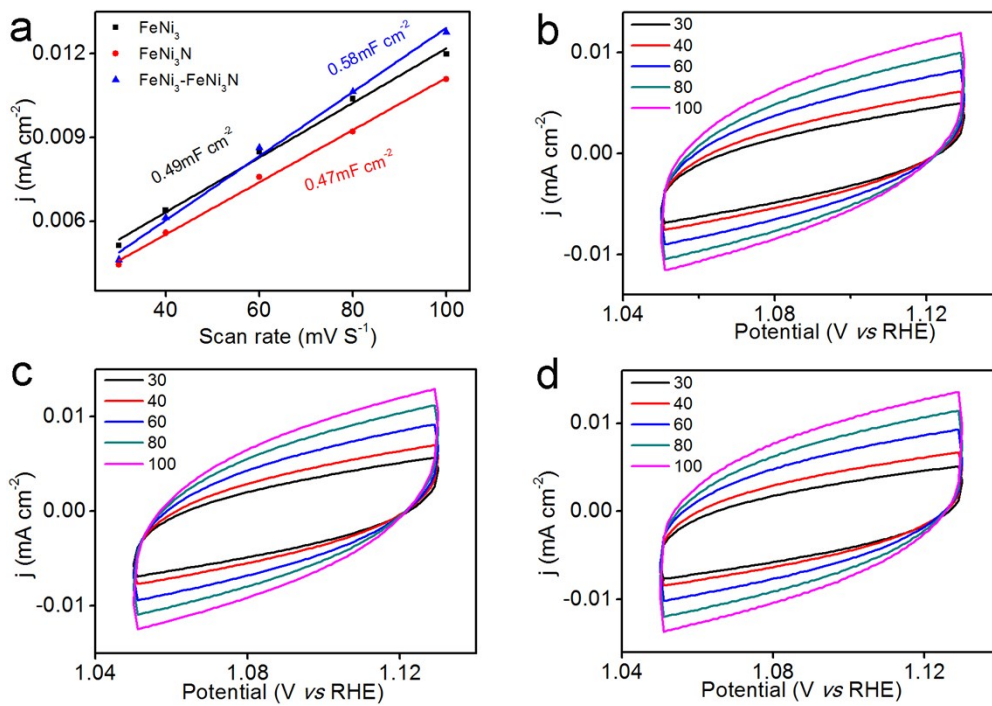


Figure S7. (a) The C_{dl} of different catalysts. (b-d) Cyclic voltammograms with a scan rate of 30, 40, 60, 80, and 100 mV s^{-1} in 1.0 M KOH for (b) FeNi₃, (c) FeNi₃N, (d) FeNi₃-FeNi₃N.

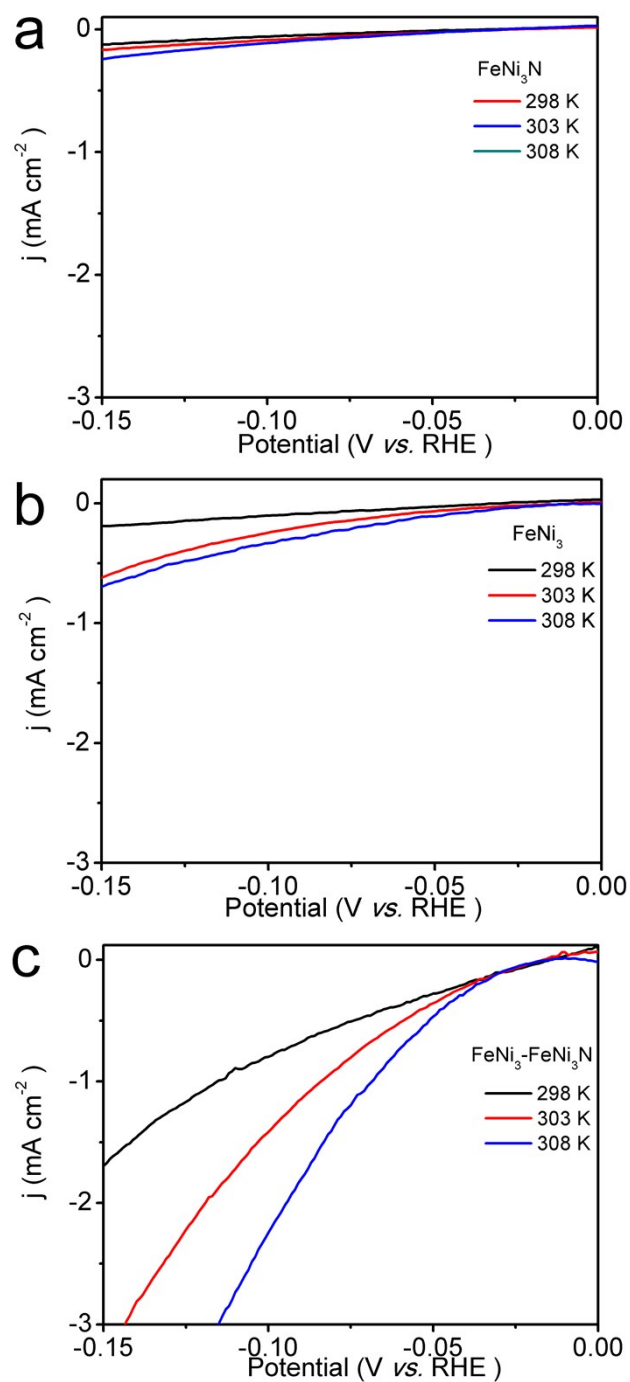


Figure S8. Arrhenius plot corresponding to HER: inverse temperature versus the natural log of the exchange current density for the samples.

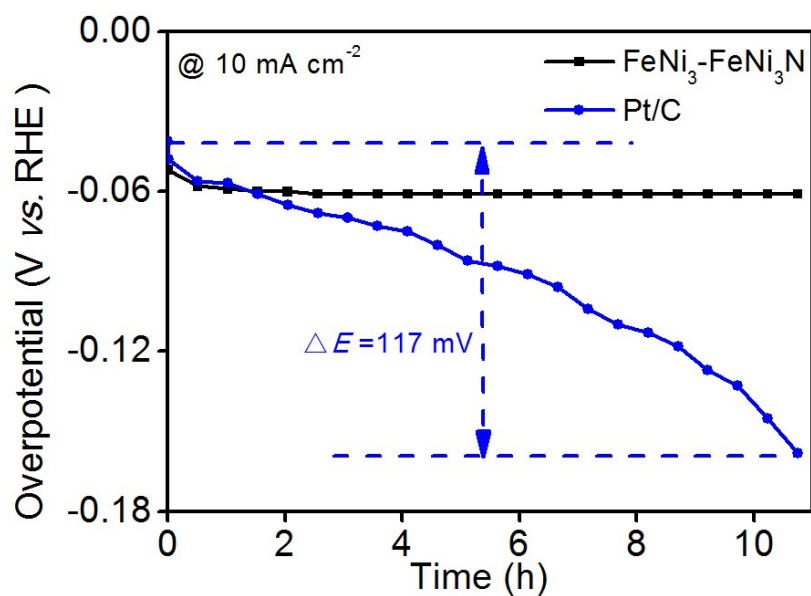


Figure S9. Durability results of FeNi₃-FeNi₃N and Pt/C in constant potential testing for HER.

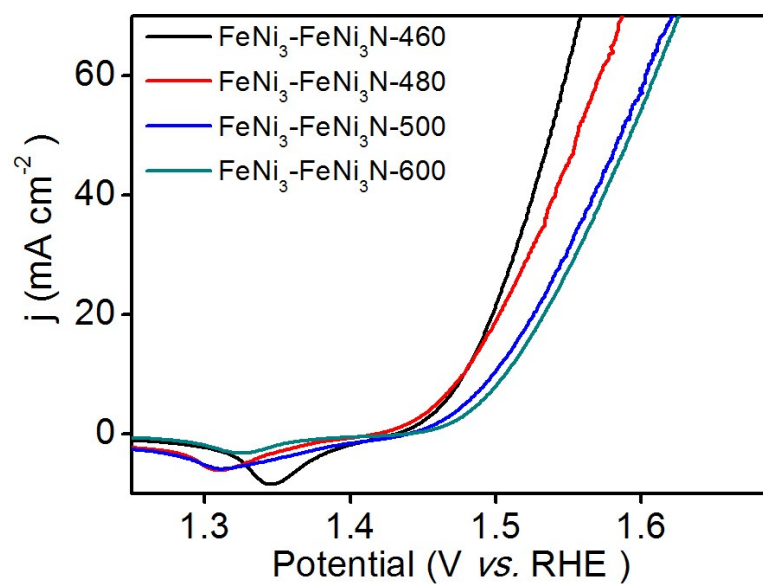


Figure S10. LSV polarization curves of the FeNi₃-FeNi₃N at different calcination temperatures for OER.

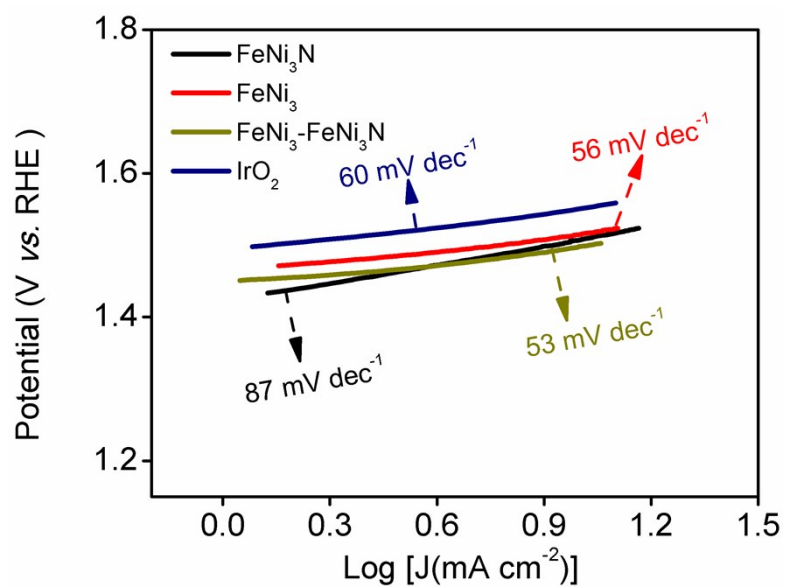


Figure S11. Tafel plots for the samples towards OER.

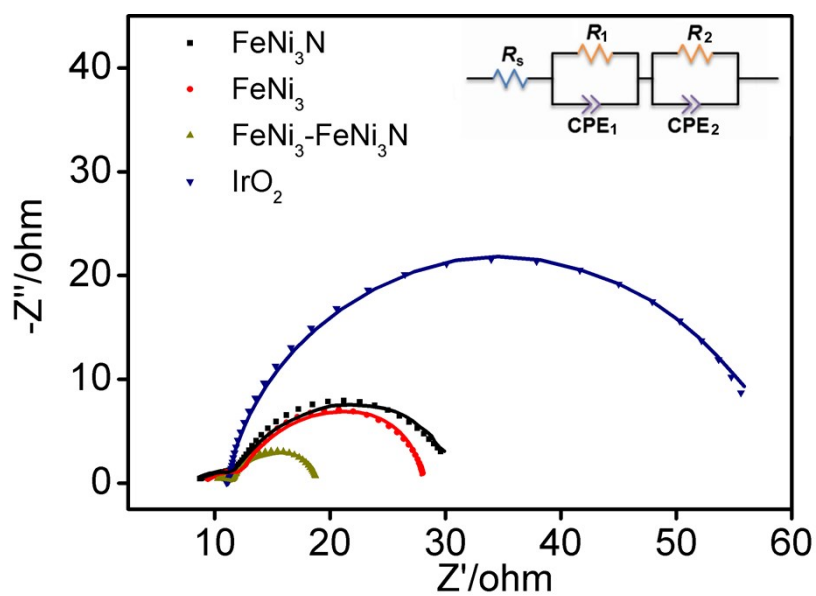


Figure S12. EIS curves of FeNi₃-FeNi₃N, FeNi₃, FeNi₃N and IrO₂ recorded during oxygen evolution at 1.5 V. (R₁: The material resistance; R₂: the charge transfer resistance)

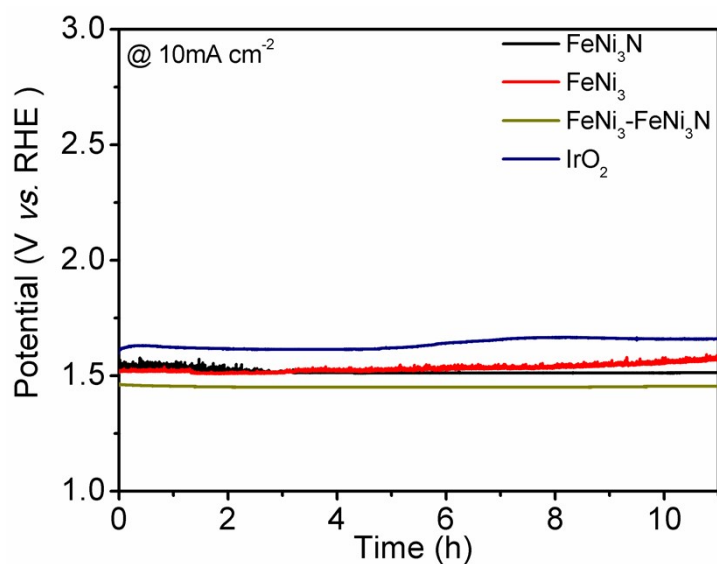


Figure S13. Durability results of samples for OER at 10 mA cm^{-2} .

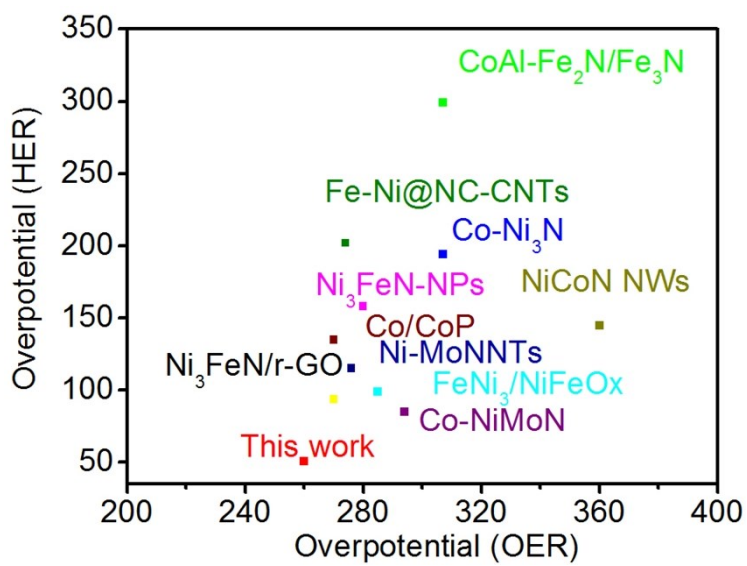


Figure S14. Comparison of the overpotential of OER and HER at current density of 10 mA cm^{-2} for $\text{FeNi}_3\text{-FeNi}_3\text{N}$ with other recent reported bifunctional electrocatalysts.

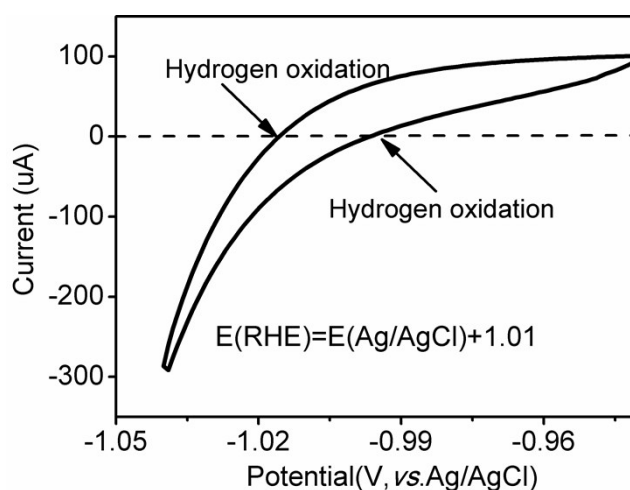


Figure S15. CV curves for RHE calibration in H_2 -saturated 1.0 M KOH at 1.0 mV.

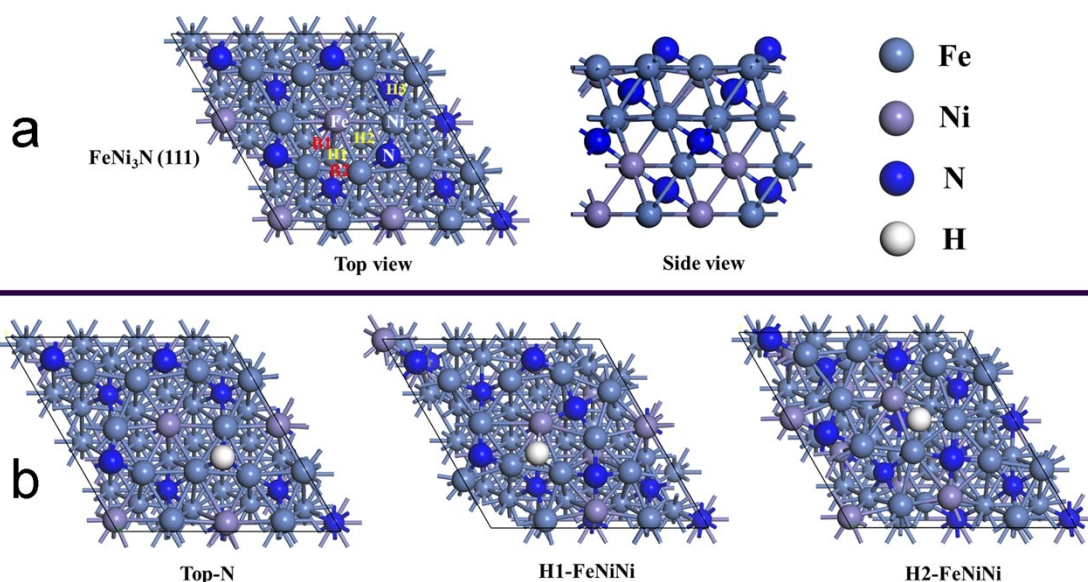


Figure S16. (a) The optimized structure of $\text{FeNi}_3\text{N}(111)$ and possible adsorption sites of H^* on it. (b) Configurations of H^* adsorption on the $\text{FeNi}_3\text{N}(111)$ surface after relaxation.

For $\text{FeNi}_3\text{N}(111)$ surface, we sampled eight possible adsorption sites of H^* for evaluating the correlative $\Delta G(\text{H}^*)$ values involving the Fe/Ni/N top sites (denoted as Fe/Ni/N), Fe-Ni/Ni-Ni bond sites (B1/B2) and Fe-Ni-Ni/Ni-Ni-Ni hollow sites (H1~H3). Finally, three structures are obtained with adsorption of H^* at Top-N and H1-H2 sites, as illustrated in Figure S12 and Table S3.

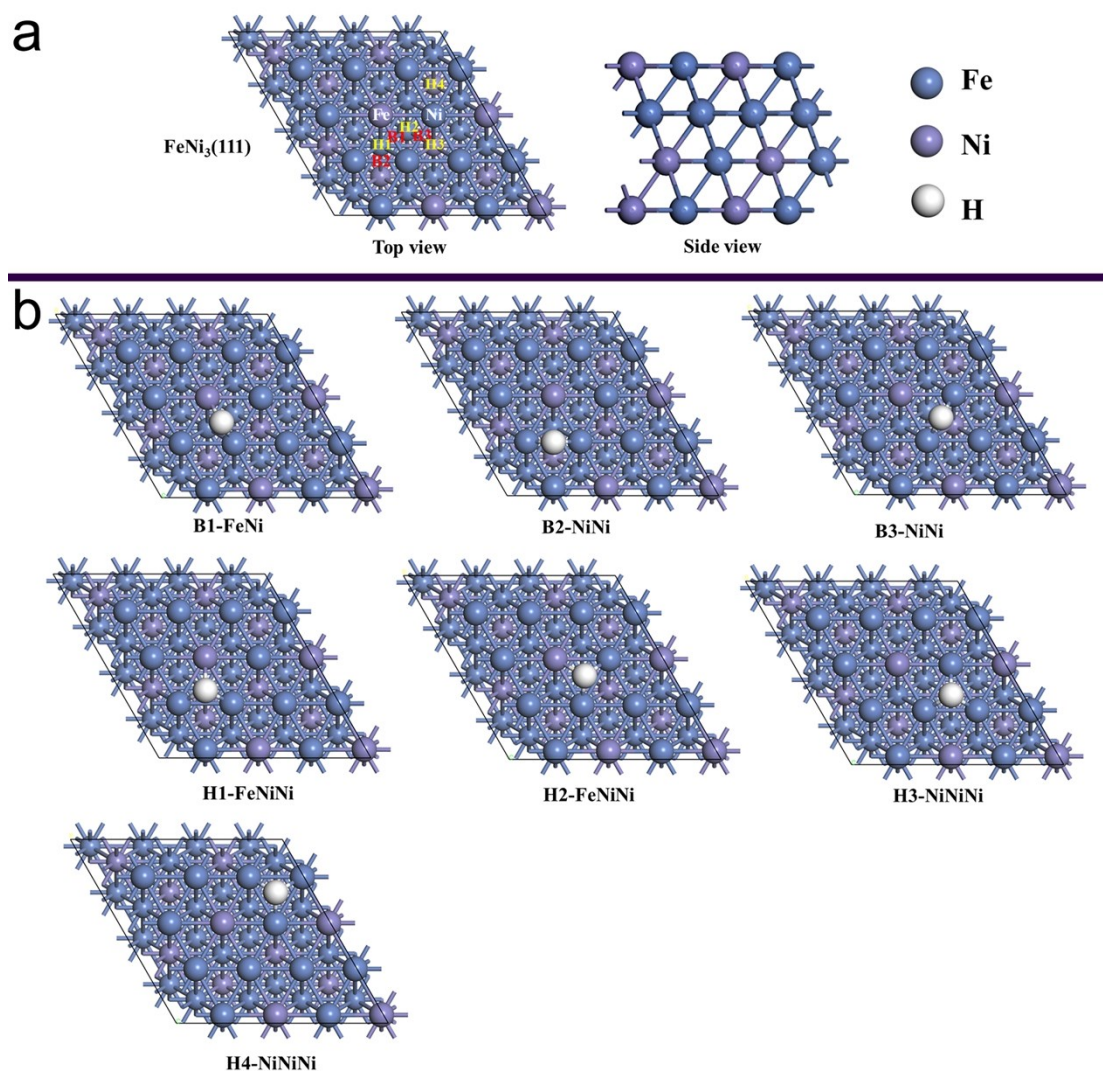


Figure S17. (a) The optimized structure of $\text{FeNi}_3(111)$ and possible adsorption sites of H^* on it. (a) Configurations of H^* adsorption on the $\text{FeNi}_3(111)$ surface after relaxation.

As displayed in the Figure S13 and Table S4, we sampled nine adsorption sites of H^* on $\text{FeNi}_3(111)$ surface, involving the Fe/Ni top sites (denoted as Fe/Ni), Fe-Ni/Ni-Ni bond sites (B1~B3) and Fe-Ni-Ni/Ni-Ni-Ni hollow sites (H1~H4). Ultimately, seven configurations with adsorbed H^* at B1~B3 and H1~H4 are obtained.

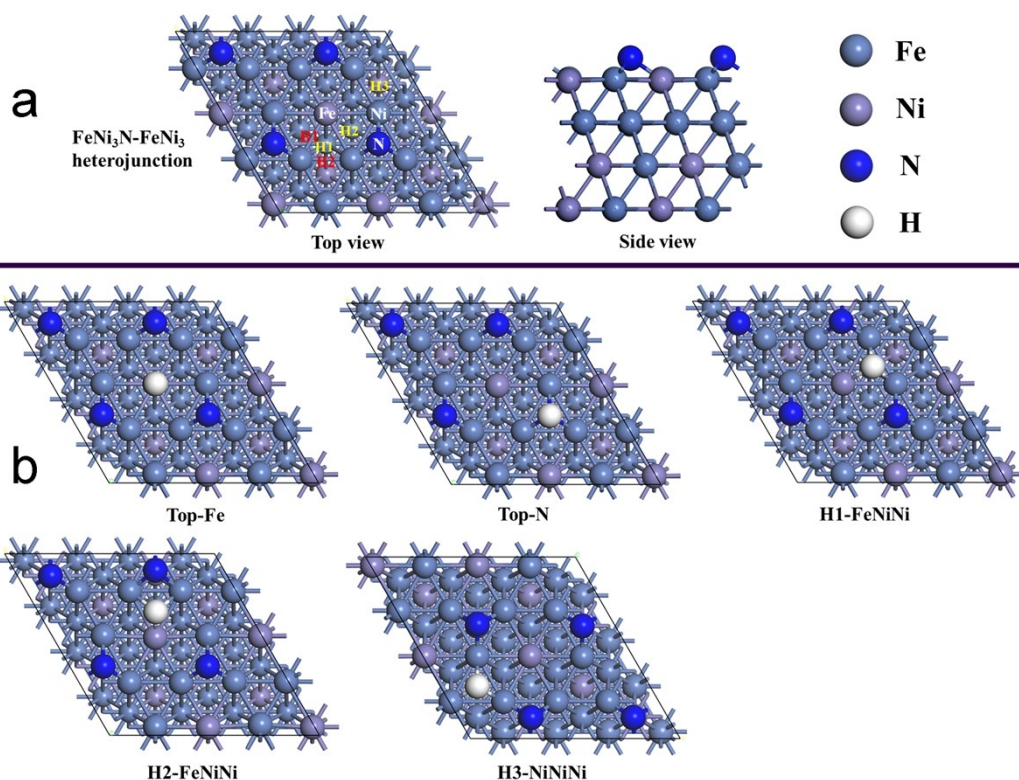


Figure S18. (a) The optimized structure of FeNi₃-FeNi₃N and possible adsorption sites of H* on it. (b) Configurations of H* adsorption on the FeNi₃-FeNi₃N surface after relaxation.

For FeNi₃-FeNi₃N heterostructure surface, we sampled eight possible adsorption sites of H*, involving the Fe/Ni/N top sites (denoted as Fe/Ni/N), Fe-Ni/Ni-Ni bond sites (B1-B2) and Fe-Ni-Ni/Ni-Ni-Ni hollow sites (H1~H3). Ultimately, five structures are obtained with adsorption of H* at Top-Fe, Top-N and H1~H3 sites, as illustrated in Figure S14 and Table S5.

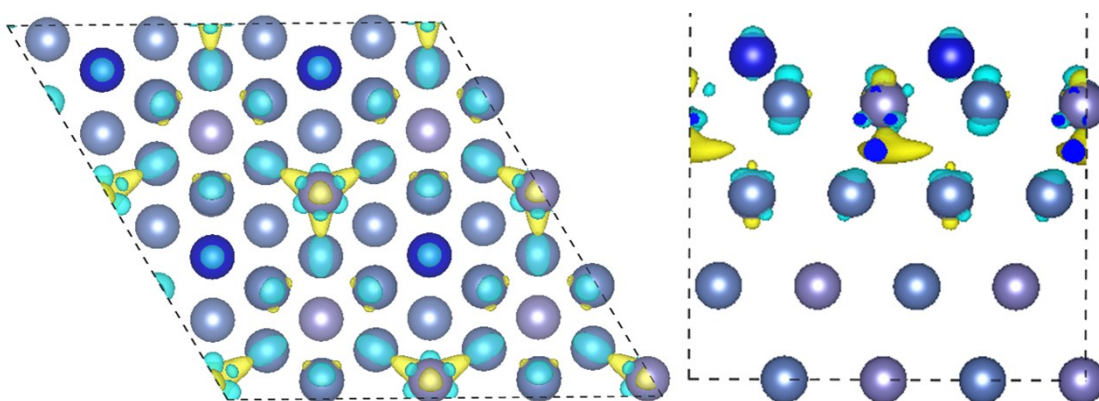


Figure S19. Calculated charge density of FeNi₃-FeNi₃N. Yellow and blue areas represent increase and reduction of charge density, respectively. The cutoff of the density-difference isosurfaces is equal to 0.01 electrons/Å³.

Table S1. Summary of reported electrocatalysts for HER in 1.0 KOH.

Samples	overpotential @ η 10 (mV)	overpotential @ η 20 (mV)	overpotential @ η 100 (mV)	Ref.
FeNi ₃ -FeNi ₃ N	51	86	215	This work
FeNi ₃ /NiFeOx	99	-	-	13
Ni ₃ FeN/r-GO	94	-	-	6
Mo-doped Ni ₃ S ₂		-	278	14
NixCo _{3-x} S ₄ /Ni ₃ S ₂ /NF	136	-	258	15
V-Ni ₃ S ₂ -NW	-	203	-	16
Fe17.5%-Ni ₃ S ₂ /NF	47	222	249	17
MoS ₂ -Ni ₃ S ₂	98	151	191	18
HNRs/NF				
Ni ₅ Fe LDH@NF	210	230	270	19
NiFeMo LDH/NF	-	-	276	20

Table S2. Electrochemical impedance spectroscopy analysis at $\eta = -70$ mV and the electrochemical active surface area (ECSA).

Samples	R _s (ohm)	R ₂ (ohm)	ECSA (m ² g ⁻¹ _{cat})
FeNi ₃ N	11.4	238.4	5.7
FeNi ₃	11.4	67.4	6.0
FeNi ₃ -FeNi ₃ N	11.2	55.2	7.1

Table S3. ΔE_{ads} , ΔZPE and ΔG_{ads} values of the H* at different adsorption sites on FeNi₃N (111) surface.

Adsorption site	$\Delta E(\text{H}^*)/\text{eV}$	$\Delta ZPE/\text{eV}$	$\Delta G(\text{H}^*)/\text{eV}$
Top-N	-1.34	0.18	-0.88
H1-FeNiNi	-1.90	0.12	-1.50
H2-FeNiNi	-2.64	0.14	-2.22

Table S4. ΔE_{ads} , ΔZPE and ΔG_{ads} values of the H* at different adsorption sites on FeNi₃(111) surface.

Adsorption site	$\Delta E(\text{H}^*)/\text{eV}$	$\Delta ZPE/\text{eV}$	$\Delta G(\text{H}^*)/\text{eV}$
B1-FeNi	-0.42	0.01	-0.13
B2-NiNi	-0.54	0.01	-0.25
B3-NiNi	-0.50	0.02	-0.20
H1-FeNiNi	-0.60	0.04	-0.28
H2-FeNiNi	-0.62	0.05	-0.29
H3-NiNiNi	-0.66	0.04	-0.34
H4-NiNiNi	-0.64	0.04	-0.32

Table S5. ΔE_{ads} , ΔZPE and ΔG_{ads} values of the H* at different adsorption sites on FeNi₃N-FeNi₃ surface.

Adsorption site	$\Delta E(\text{H}^*)/\text{eV}$	$\Delta ZPE/\text{eV}$	$\Delta G(\text{H}^*)/\text{eV}$
Top-Fe	0.38	-0.01	0.65
Top-N	-1.18	0.16	-0.74
H1-FeNiNi	-0.22	0.05	0.11
H2-FeNiNi	-0.27	0.00	0.01
H3-NiNiNi	-0.40	0.05	-0.07

Table S6. Series resistance (R_s) and charge transfer resistance (R_{ct}) based on the Nyquist plots in Figure S9 during oxygen evolution at $\eta = 270$ mV.

Samples	R_s (ohm)	R_2 (ohm)
FeNi ₃ N	11.3	18.8
FeNi ₃	11.4	16.6
FeNi ₃ -FeNi ₃ N	11.6	7.0
IrO ₂	11.1	54.0

Table S7. Summary of reported overall-water-splitting performance of related catalysts in 1.0 M KOH.

Samples	Mass loading (mg cm⁻²)	Current density (mA mg⁻¹) at 1.50 V	E_{Cell} (V) at 10 mA cm⁻²	Ref.
FeNi ₃ -FeNi ₃ N	5.0	2.0	1.50	This work
Ni ₃ FeN/r-GO	-	-	1.59	6
NiFeO _x /CFP	3.0	2.3	1.51	21
Ni ₂ Fe ₁ -O	6.1	1.1	1.64	22
NiFe-NP	3.0	2.0	1.55	23
Fe-Ni@NC-CNTs	1.0	1.0	1.75	24
δ-FeOOH	-	-	1.62	25
NiFeLDH@NiCoP/NF	2.0	1.0	1.57	26
Ni ₂ P/NiOOH	2.0	1.3	1.57	27
CoP/NCNHP	2.0	1.8	1.64	28
am-Fe-Bi/NF	-	-	1.62	29

Note: All datas of the samples were compared without iR-compensation.

References

1. G. Kresse and J. Furthmüller, *Physical review B*, 1996, 54, 11169.
2. G. Kresse and J. Furthmüller, *Computational materials science*, 1996, 6, 15-50.
3. P. E. Blöchl, *Physical review B*, 1994, 50, 17953.
4. G. Kresse and D. Joubert, *Physical review b*, 1999, 59, 1758.
5. J. P. Perdew, K. Burke and M. Ernzerhof, *Physical review letters*, 1996, 77, 3865.
6. Y. Gu, S. Chen, J. Ren, Y. A. Jia, C. Chen, S. Komarneni, D. Yang and X. Yao, *ACS Nano*, 2018, 12, 245-253.
7. P. Lyu and P. Nachtigall, *Catalysis Today*, 2019, 345, 220-226.
8. X. Zhang, Y. Zhao, X. Jia, Y. Zhao, L. Shang, Q. Wang, G. I. Waterhouse, L. Z. Wu, C. H. Tung and T. Zhang, *Advanced Energy Materials*, 2018, 8, 1702780.
9. H. Li, S. Chen, H. Lin, X. Xu, H. Yang, L. Song and X. Wang, *Small*, 2017, 13, 1701487.
10. Yan, Haijing, Xie, Ying, Jiao, Yanqing, Wu, Aiping, Tian and Chungui, *Advanced Materials*, 2018, 30(2), 1704156.
11. J. K. Nørskov, T. Bligaard, A. Logadottir, J. Kitchin, J. G. Chen, S. Pandelov and U. Stimming, *Journal of The Electrochemical Society*, 2005, 152, J23-J26.
12. L. L. Feng, G. Yu, Y. Wu, G. D. Li, H. Li, Y. Sun, T. Asefa, W. Chen and X. Zou, *Journal of the American Chemical Society*, 2015, 137, 14023-14026.
13. X. Yan, L. Tian, K. Li, S. Atkins, H. Zhao, J. Murowchick, L. Liu and X. Chen, *Advanced Materials Interfaces*, 2016, 3, 1600368.
14. Z. Cui, Y. Ge, H. Chu, R. Baines, P. Dong, J. Tang, Y. Yang, P. M. Ajayan, M. Ye and J. Shen, *Journal of Materials Chemistry*, 2017, 5, 1595-1602.
15. Y. Wu, Y. Liu, G. Li, X. Zou, X. Lian, D. Wang, L. Sun, T. Asefa and X. Zou, *Nano Energy*, 2017, 35, 161-170.
16. Y. Qu, M. Yang, J. Chai, Z. Tang, M. Shao, C. T. Kwok, M. Yang, Z. Wang, D. H. C. Chua and S. J. Wang, *ACS Applied Materials & Interfaces*, 2017, 9, 5959-5967.
17. G. Zhang, Y.-S. Feng, W.-T. Lu, D. He, C.-Y. Wang, Y.-K. Li, X.-Y. Wang and F.-F. Cao, *ACS Catalysis*, 2018, 8, 5431-5441.
18. Y. Yang, K. Zhang, H. Lin, X. Li, H. C. Chan, L. Yang and Q. Gao, *ACS Catalysis*, 2017, 7, 2357-2366.
19. Y. Zhang, Q. Shao, Y. Pi, J. Guo and X. Huang, *Small*, 2017, 13, 1700355.
20. N. Han, F. Zhao and Y. Li, *Journal of Materials Chemistry*, 2015, 3, 16348-16353.
21. H. Wang, H.-W. Lee, Y. Deng, Z. Lu, P.-C. Hsu, Y. Liu, D. Lin and Y. Cui, *Nature Communications*, 2015, 6, 1-8.
22. C. Dong, T. Kou, H. Gao, Z. Peng and Z. Zhang, *Advanced Energy Materials*, 2018, 8, 1701347.
23. B. H. R. Suryanto, Y. Wang, R. K. Hocking, W. Adamson and C. Zhao, *Nat Commun*, 2019, 10, 5599.
24. X. Zhao, P. Pachfule, S. Li, J. R. J. Simke, J. Schmidt and A. Thomas, *Angew Chem Int Ed Engl*, 2018, 57, 8921-8926.
25. B. Liu, Y. Wang, H. Q. Peng, R. Yang, Z. Jiang, X. Zhou, C. S. Lee, H. Zhao and W. Zhang, *Adv Mater*, 2018, DOI: 10.1002/adma.201803144, e1803144.
26. H. Zhang, X. Li, A. Hähnel, V. Naumann, C. Lin, S. Azimi, S. L. Schweizer, A. W. Maijenburg and R. B. Wehrspohn, *Advanced Functional Materials*, 2018, 28, 1706847.
27. H. Sun, X. Xu, Z. Yan, X. Chen, F. Cheng, P. S. Weiss and J. Chen, *Chemistry of Materials*, 2017, 29, 8539-8547.
28. Y. Pan, K. Sun, S. Liu, X. Cao, K. Wu, W. C. Cheong, Z. Chen, Y. Wang, Y. Li, Y. Liu, D. Wang, Q. Peng, C. Chen and Y. Li, *J Am Chem Soc*, 2018, 140, 2610-2618.
29. W. Zhao, T. Xu, T. Li, Y. Wang, H. Liu, J. Feng, S. Ding, Z. Li and M. Wu, *Small*, 2018, 14, e1802829.